ACS Energy Letters

http://pubs.acs.org/journal/aelccp

LETTER

Stabilizing a Li−Mn−O Cathode by Blocking Lattice O Migration through a Nanoscale Phase Complex

Weiyuan Huang, Mingjian Zhang,* Mingyuan Ge,* Shunning Li,* Lin Xie,* Zhefeng Chen, Gang Wang, Junhao Lin, Jimin Qiu, Lei Yu, Jianguo Wen, Guo-Xi Ren, Cong Lin, Wenguang Zhao, Haibiao Chen, and Feng Pan*

Cite This: *ACS Energy Lett.* 2023, 8, 901−908

Read Online

ABSTRACT: Among all intercalation cathodes for Li-ion batteries, Li−Mn−O layered oxides offer the highest initial energy density at the lowest cost, due to the joint contribution from cationic and anionic redox chemistry. However, the poor cycling capability, resulting from the continuous lattice O loss at high potentials (>4.5 V), hinders practical applications. Herein, we employed phase complex engineering to obtain a new Li−Mn−O nanohybrid cathode featuring the uniform and coherent integration of layered nanodomains and spinel nanodomains. The combination of DFT calculations, synchrotron-based transmission X-ray microscopy, *in situ* differential electrochemical mass spectrometry, *in situ* synchrotron XRD, and electrochemical tests demonstrated that the O migration path in layered nanodomains was blocked by the neighboring spinel nanodomains with a higher oxygen vacancy migration energy, thus effectively suppressing the irreversible lattice O loss at high potentials and enhancing the cycling stability in both capacity and average voltage. The strategy is experimentally demonstrated to be effective and it leads to a new path for developing stable high-energy-density cathode materials.

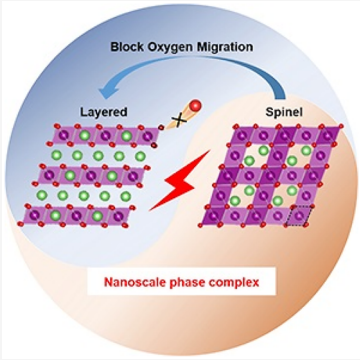

The development of battery technology is largely driven by the discovery of new materials. For Li-ion batteries, there have been always demands on the cathode to continually improve the reversible capacity, rate capability, and cycling stability.[1−3] The capacities of current commercial cathode materials, including $LiFePO_4$,[4,5] $LiMn_2O_4$,[6,7] $LiCoO_2$,[8,9] and $LiNi_xCo_yMn_{1-x-y}O_2$/$LiNi_xCo_yAl_{1-x-y}O_2$ (NCM/NCA, $0 < x, y < 1$),[10,11] are largely restricted by the redox of transition-metal cations, and they are below 220 mA h g^{-1} in practice, corresponding to an energy density of <800 W h kg^{-1}.[12] An anionic redox reaction in Li-rich layered oxide cathodes was discovered to be able to boost the practical capacity to >250 mA h g^{-1} and the energy density to >1000 W h kg^{-1}.[13−16] Previous studies revealed that oxygen redox commonly occurs in both NCM and Li-rich cathodes when they are charged over the critical voltage, which can be attributed to the Li−O−Li or Li−O−vacancy configurations (generated at a deep delithiation state in NCM).[17−20] Li-rich layered oxides are typically composed of two layered phases, Li_2MnO_3 and $LiTMO_2$ (TM = Ni, Co, Mn). Li_2MnO_3 with a monoclinic symmetry (space group $C2/m$) shows a high theoretical capacity (up to 459 mA h g^{-1}) but a very poor practical capacity of <200 mA h g^{-1} due to the irreversible O loss.[21−23] $LiTMO_2$ with a rhombohedral symmetry (space group $R\bar{3}m$) exhibits a relatively low theoretical capacity (<200 mA h g^{-1}) with TM redox while having a relatively stable structure. The structural integration of these two phases combines TM redox and O redox together and delivers a high reversible capacity of >250 mA h g^{-1}.[24,25] This phase complex engineering strategy has proved to be effective in stabilizing O-redox-related intercalation cathodes, although Li-rich layered oxides still suffer from issues such as capacity/voltage fading.[26−29]

Following the phase complex engineering strategy, here we design a layered-spinel nanohybrid architecture for a Li−Mn−O cathode (denoted LS-LMO) based on an in-depth understanding of the intercalation structures and DFT calculations. As shown in Figure 1a, layered-phase Li_2MnO_3 (represented by blue squares) and spinel phase $LiMn_2O_4$ (represented by pink squares) possess the same hexagonal-

Received: November 5, 2022
Accepted: December 21, 2022
Published: January 6, 2023

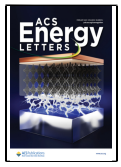

https://doi.org/10.1021/acsenergylett.2c02507
ACS Energy Lett. 2023, 8, 901−908

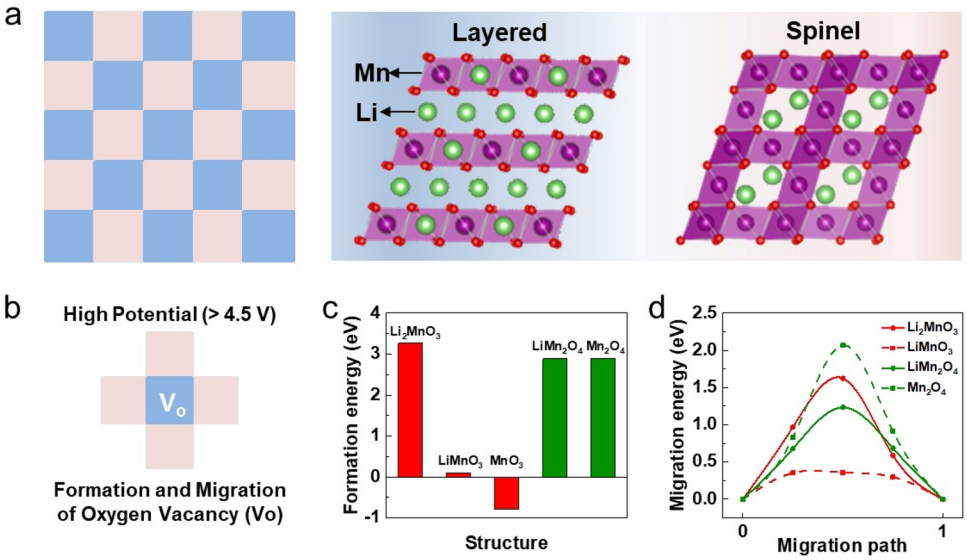

Figure 1. Structure design of biphasic phase complex cathodes. (a) Schematic illustration of the layered-spinel nanohybrid architecture. The layered and spinel phases are represented by the blue and pink squares, respectively. (b) Formation and migration of an oxygen vacancy (V_O) in the layered-spinel nanohybrid at high potentials (>4.5 V). V_O formation energies (c) and migration energies (d) for layered Li_2MnO_3, half-delithiated Li_2MnO_3 ($LiMnO_3$), fully delithiated Li_2MnO_3 (MnO_3), spinel $LiMn_2O_4$, and fully delithiated $LiMn_2O_4$ (Mn_2O_4).

close-packed anionic oxygen framework, which ensures the structural compatibility. Most importantly, they are complementary in electrochemical performance at high potentials (>4.5 V). The layered phase Li_2MnO_3 is unstable due to the irreversible O redox and continuous O loss,[30] while the spinel phase $LiMn_2O_4$ is stable since no O redox is involved at high potentials (even up to 4.8 V). In the delithiated layered phases (Li_2MnO_3 and MnO_3), oxygen vacancies (V_O) are facile and even spontaneous to form due to the small and negative values of the V_O formation energy (0.10 and −0.79 eV for $LiMnO_3$ and MnO_3, respectively; Figure 1c) and also easily migrate due to the small V_O migration energy (0.36 eV for $LiMnO_3$; Figure 1d). When they are surrounded by the delithiated spinel phase Mn_2O_4 (Figure 1b), the vacancies in the layered phase have difficulty in migrating due to the higher V_O formation energy (2.90 eV for Mn_2O_4; Figure 1c and Figure S1) and higher V_O migration energy (2.07 eV for Mn_2O_4; Figure 1d), which would improve the structural stability of the Li_2MnO_3 layered phase at high potentials to a great extent. Besides, the layered phase mainly undergoes a volumetric expansion during a charge, while the spinel phase mainly undergoes a volumetric contraction during a charge.[7,31] Such complementary behaviors benefit reducing the volumetric and strain changes during charge/discharge, which have recently been identified as the origin of the structural degradation in Li-rich layered cathodes.[32] In brief, such a design of a layered-spinel nanohybrid architecture is expected to solve the fundamental concern of the irreversible O redox and deliver enhanced performance. Though there have been some reports on layered/spinel heterostructures,[23−36] most of these materials were designed in the form of a core−shell architecture with a spinel shell on the layered core. The nonuniform coating and the spallation of the spinel shell during repeated cycles still jeopardize the cycling stability.[37,38]

Herein, the layered-spinel biphasic complex Li−Mn−O cathode was successfully prepared by the ion-exchange method. Since the spinel structure is integrated into the layered structure coherently at the nanoscale and effectively blocks the O migration route, it exhibits ultrahigh reversible capacities (>440 mA h g^{-1}) with decent cycling stability in a wide voltage region. Our work opens a new path for developing high-performance cathodes through a nano phase complex strategy.

LS-LMO exhibits a morphology of spherical-like secondary particles with a size of about 1 μm, composed of primary nanoparticles with a size of 50−100 nm (Figure S2a). The molecular formula was determined to be $Li_{1.13}Mn_{0.75}O_2$ by ICP-OES (Table S1). The average structure was characterized by combining X-ray (XRD) and neutron diffraction (ND) data (Figure 2a). A Rietveld refinement was performed using two phases, a layered model (space group $C2/m$) and a spinel model (space group $Fd\bar{3}m$). The weight ratio of layered and spinel phases in LS-LMO was determined to be 0.83:0.17, confirming the coexistence of both phases. The detailed structural parameters are given in Tables S2−S4. Different from the stoichiometric Li_2MnO_3 and $LiMn_2O_4$, the layered-phase component shows serious Li/Mn mixing in the Mn layers (Table S3), and the spinel phase component presents a small amount of of Li/Mn mixing at Li (8a) and Mn (16d) sites (Table S4), which manifest the complex effect of two phases at the atomic level.

The local structure was investigated by high-resolution transmission electron microscopy (HRTEM). As shown in Figure S2b, two regions were selected in HRTEM images to perform fast Fourier transform (FFT). The FFT patterns from the blue regions represent a typical layered structure like that of Li_2MnO_3 (Figure S3a),[39,40] However, the FFT patterns from the pink regions represent a spinel-like structure like that of $LiMn_2O_4$ (Figure S3b), indicating the layered-spinel hybridization within the individual primary particle for LS-LMO, which is further confirmed by the HAADF-STEM image (Figure S4). The HRTEM images in Figure 2b,c show that the layered structure along the [100] direction (marked by a blue shadow) is hybridized with the spinel-like structure along the [211] direction (marked by a pink shadow), with a form of intralayer coherence at the nanoscale, consistent with the

https://doi.org/10.1021/acsenergylett.2c02507
ACS Energy Lett. 2023, 8, 901−908

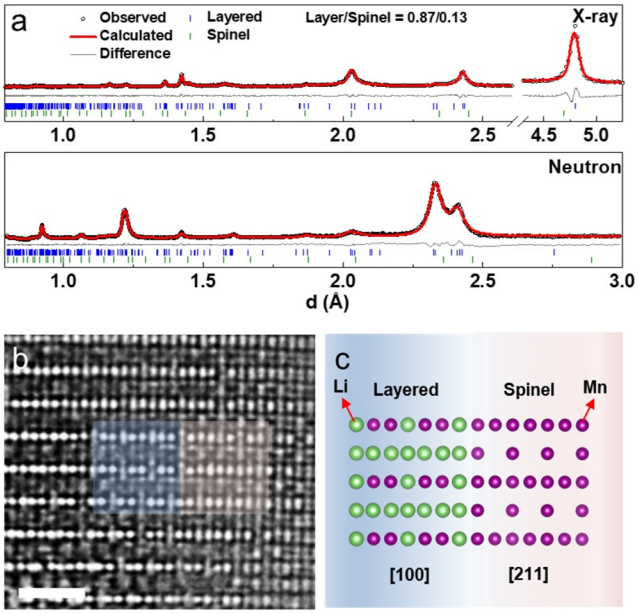

Figure 2. Examination of a layered-spinel biphasic nanoscale complex structure. (a) X-ray and neutron diffraction patterns as well as the combined Rietveld refinement for LS-LMO. R_{wp} = 6.58%. Atomic-resolved HRTEM image for LS-LMO (b) and the corresponding phase structural diagram for the selected regions (c). Scale bar: 1 nm.

structure design in Figure 1a. Besides, continuous bright spots were observed in the layered regions, indicating serious Li/Mn mixing in the Mn layers, consistent with the diffraction results above.

The electrochemical performance of LS-LMO is shown in Figure 3. First, we compare the charge−discharge profile of LS-LMO with those of layered Li_2MnO_3 and spinel $LiMn_2O_4$ in the voltage range of 1.3−4.9 V in Figure 3a. LS-LMO presents a long plateau at around 4.6 V similar to that of Li_2MnO_3 (blue dashed rectangle) during the first charge, coming from the contribution of oxygen redox in the layered component.[41] There are also two short plateaus at around 4.0 and 2.8 V like those of $LiMn_2O_4$ (red dashed rectangles), coming from Mn redox in the spinel component. We can deduce the ratio between the layered and spinel phases to be 0.85:0.15 according to the respective capacity contribution during the first charge, consistent with the diffraction refinement results above. Surprisingly, due to the synergistic effect of two phases, the initial discharge capacity is as high as 442 mA h g^{-1}, close to the theoretical capacity of Li_2MnO_3 (462 mA h g^{-1}) and equivalent to an ultrahigh energy density of 1270 W h kg^{-1} (calculated according to the weight of active material in the cathode). The extra capacity at the low-voltage range (<2 V) can be ascribed to the insertion of more Li^+ into tetrahedral sites in Li slabs with Mn reduction, consistent with previous literature reports.[42−44] The corresponding CV curves in Figure S5 further confirm the two-phase synergistic effect on the electrochemical behaviors. Besides, LS-LMO delivered a discharge capacity of 388 mA h g^{-1} at 50 mA g^{-1} and of 118 mA h g^{-1} at 10 A g^{-1}, exhibiting superior rate capability (Figure S6). The cycling stability was compared at 500 mA g^{-1} (Figure 3b,c). LS-LMO retains a reversible capacity of 204 mA h g^{-1} after 150 cycles, remarkably superior to Li_2MnO_3. Also, the voltage decay in LS-LMO was only 0.065 V after 150

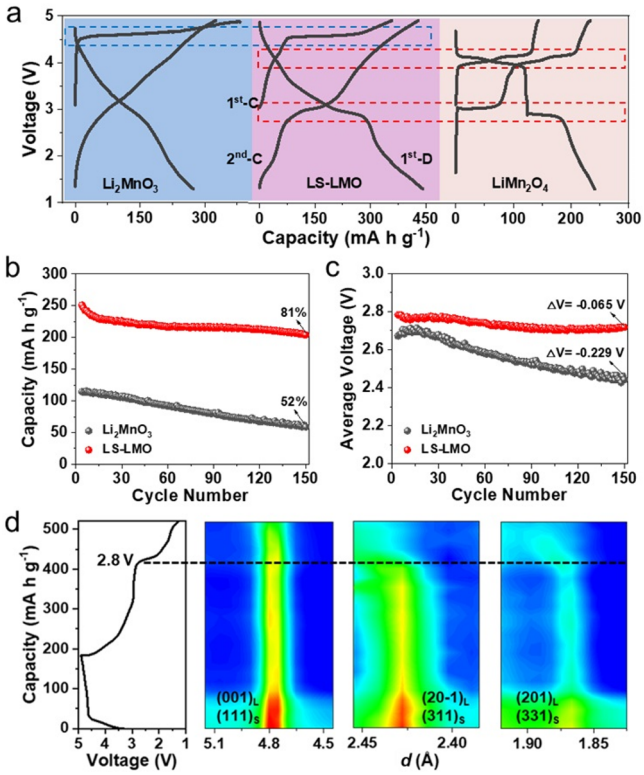

Figure 3. Superior electrochemical performance. (a) The first charge/discharge (1st-C/1st-D) and second charge (2nd-C) profiles for LS-LMO, Li_2MnO_3, and $LiMn_2O_4$ in the range 1.3−4.9 V at 10 mA g^{-1}. The change of the discharge capacity (b) and the average voltage (c) for LS-LMO and Li_2MnO_3 on cycling at 500 mA g^{-1}. (d) Contour plot of *in situ* synchrotron XRD patterns during the first cycle of LS-LMO at 80 mA g^{-1}.

cycles, almost 1 order of magnitude smaller than that in Li-rich Mn-based oxides.[45]

To determine the structure change of LS-LMO during charge/discharge, *in situ* synchrotron XRD patterns were collected during the first cycle of LS-LMO. As shown in Figure 3d, the overlapping layered-spinel peaks $(001)_L/(111)_S$, $(20-1)_L/(311)_S$, and $(201)_L/(331)_S$ did not split, and there was no noticeable peak shift during charge/discharge, demonstrating the excellent structure stability of the nanoscale phase composite since the volumetric and strain changes in the layered phase and spinel phase are complementary to a great extent during charge/discharge.[7,31] After discharging below 2.8 V, the peaks gradually attenuated and shifted slightly to the high-*d* direction. The changes suggest a phase transition due to the J-T distortion, although the J-T effect has been largely inhibited.

In brief, through a layered-spinel phase complex at the nanoscale, LS-LMO exhibited better cycling performance and superior rate capability than the benchmark layered Li_2MnO_3 cathode, indicating the great success of such nanohybrid structure in enhancing the electrochemistry.

Anionic redox is the core for implementing a high capacity and also a critical factor affecting the cycling stability for Li−Mn−O layered cathodes. To examine the influence of the nanohybrid structure on the O redox reaction, transmission X-ray microscopy (TXM) coupled with 3D X-ray absorption near-edge spectra (XANES) were employed to study the LS-LMO electrodes at different charge/discharge states. TXM

https://doi.org/10.1021/acsenergylett.2c02507
ACS Energy Lett. 2023, 8, 901−908

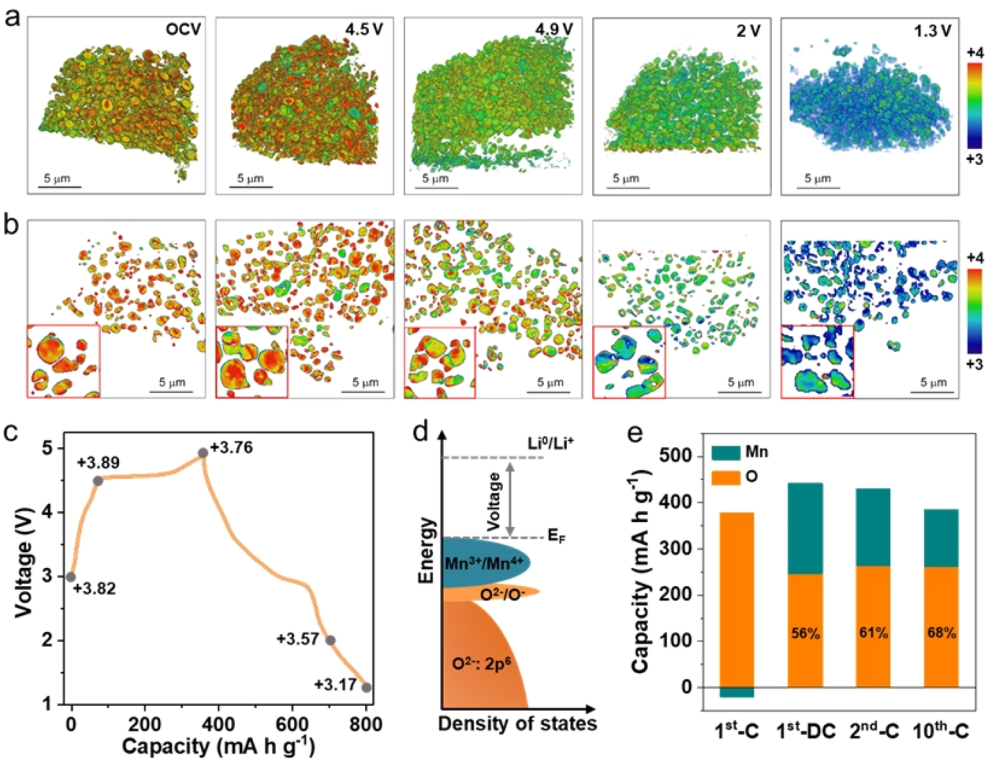

Figure 4. Reversible O redox by layered/spinel phase complex. 3D rendering (a) and the corresponding 2D slice views (b) of Mn valence state distribution for LS-LMO samples at the OCV state, on charging to 4.5 and 4.9 V, and on discharging to 2 and 1.3 V by the TXM technique. (c) Mn valence states deduced from TXM results in (a) marked in the capacity−voltage profile. (d) Schematic diagram of the density of states of Mn and O. (e) Histogram showing the contribution of Mn redox and O redox to the capacity during the first charge (1st-C), first discharge (1st-D), second charge (2nd-C) and thenth charge (10th-D), deduced from the TXM results in (a).

offers a unique capability to investigate the spatial distribution of the elemental valence state at a high resolution.[46,47] Here we probed the Mn oxidation/reduction in various states of charge/discharge (Figure 4a,b and Figures S7 and S8). Figure 4a presents a 3D rendering of Mn valence distribution at OCV, 4.5, 4.9, 2, and 1.3 V of the first cycle, respectively. The color changes from green to red then to green and eventually blue, demonstrating the gradual oxidation process of Mn cations from OCV to 4.5 V, then the partial reduction of Mn from 4.5 to 4.9 V, and further reduction of Mn during discharge. The Mn reduction at high voltage may be related to the lattice oxygen loss or the interplay between the overlapped Mn^{3+}/Mn^{4+} and O^{2-}/O^{-} states.[48−50] A similar observation was further confirmed by the 2D slice views in Figure 4b, and the insets reflect the nonuniform distribution of Mn valence within individual particles.

To quantify the changes in the valence state of Mn with charge/discharge, we counted over all the voxels in the 3D XANES and performed a fitting (Figure S7). The results were marked in the charge/discharge curves (the upper panel of Figure 4c). The small changes in Mn valence state during the first charge and first discharge are −0.06 and −0.59, respectively, which confirms the combined contribution of Mn redox and O redox to the high reversible capacities (Figure 4d). Based on the quantitative contribution of Mn redox to the capacities, we can deduce the contribution of O redox during the first cycle, the second charge, and the tenth charge (Figure 4e). It is clear that the capacity contribution from O redox is over 100% during the first charge due to the negative contribution of Mn redox (the capacity contribution of Mn reduction behavior during the charge process was defined as a negative value). It decreases to 56% at the first discharge and gradually increases to 68% until the tenth charge, hinting at the great reversibility of O redox during the subsequent stable cycling. The redox of Mn and O can be also confirmed by the Mn L-edge and O K-edge soft X-ray absorption spectra (sXAS; Figure S9).

In situ differential electrochemical mass spectrometry (DEMS) was used to capture gas evolution during cycling. As shown in Figure 5b, little CO_2 and even less O_2 release was detected at high potentials during the first charge of LS-LMO, while much more significant O_2 and CO_2 signals were noticed in Li_2MnO_3 (Figure 5a). More importantly, there is no O_2 and CO_2 detected during the second cycle in LS-LMO, in contrast to the obvious gas release in Li_2MnO_3. These results indicate that the lattice O release and carbonate-electrolyte decomposition reactions were efficiently suppressed by the nanohybrid structure, which is responsible for the enhanced reversibility of O redox and the excellent cycling stability.

The local structure changes were also examined. Figure 5c−e exhibits the local structures of Li_2MnO_3 after the 1st, 10th, and 50th cycle, respectively. The layered structure partially transformed to the spinel phase even after the first cycle, as demonstrated by the HRTEM image as well as the corresponding FFT map in Figure 5c and then underwent quick structure degradation with a serious loss of crystallization, demonstrated by the diffraction rings in FFT maps in Figure 5d,e. The increased full width at half-maximum (fwhm) of the XRD peaks after the 50th cycle further confirm the continuous structure degradation and crystallization loss of Li_2MnO_3 (Figure S10). In addition, O vacancy clusters can be observed in the lattice of Li_2MnO_3 after the 10th and 50th

https://doi.org/10.1021/acsenergylett.2c02507
ACS Energy Lett. 2023, 8, 901−908

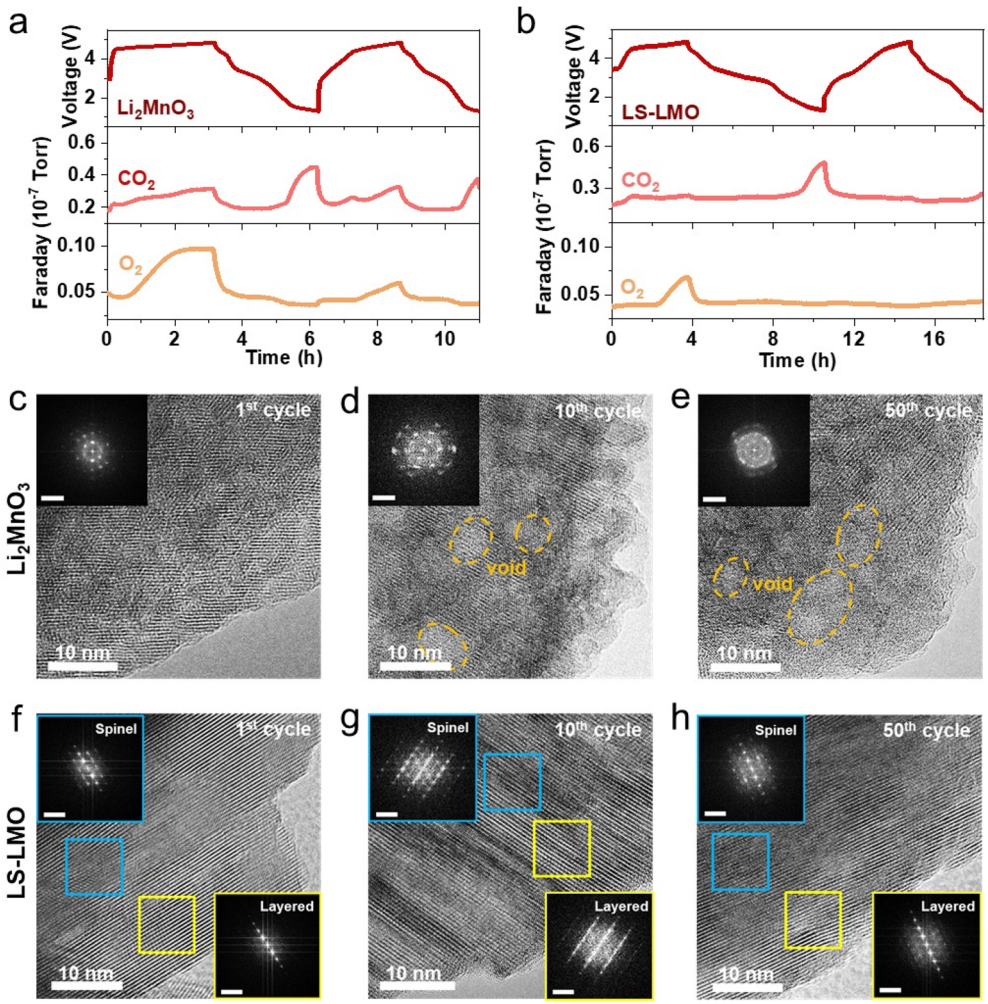

Figure 5. Structural stability of LS-LMO upon cycling. ***In situ*** **DEMS during the first two cycles of Li_2MnO_3 (a) and LS-LMO (b). HRTEM images of Li_2MnO_3 after the 1st (c), 10th (d), and 50th (e) cycles. HRTEM images of LS-LMO after the 1st (f), 10th (g), and 50th (h) cycles.**

cycles (marked by the orange dashed ellipses in Figure 5d,e), which likely originate from oxygen gas evolution and oxygen vacancy condensation.[51] In contrast, the layered nanodomains marked by yellow rectangles and the spinel nanodomains marked by blue rectangles were continually observed after the 1st, 10th, and 50th cycles (Figure 5f–h and Figure S11a), even after the 100th cycle (Figure S11b). It indicates the great structure stability of such a nanoscale complex structure, which should be related to the inhibited lattice O loss demonstrated by *in situ* DEMS and responsible for the excellent cycling stability.

The spinel-like phase unavoidably forms during the structure degradation of Li_2MnO_3.[52] To distinguish the spinel phase in LS-LMO and the spinel-like phase in cycled Li_2MnO_3, the O K-edge and Mn L-edge EELS spectra of pristine LS-LMO, LS-LMO and Li_2MnO_3 after the first cycle were collected (Figure S12). The prepeak of the O K-edge, highlighted by a dashed line, is related to the transition of the O 1s core state to the unoccupied O 2p states that are hybridized with TM 3d states.[53] It can be found that LS-LMO samples before cycling and after the first cycle exhibit an obvious prepeak signal, in contrast to the almost absent prepeak in Li_2MnO_3 after the first cycle. The Mn L-edge of the cycled Li_2MnO_3 shifts to lower energy, indicating a lower valence state of Mn compared with LS-LMO samples. These indicate that the spinel-like structure formed in the cycled Li_2MnO_3 may contain more oxygen vacancies and be close to an Mn_3O_4-type spinel with a lower Mn valence, which could not hinder further O loss and would accelerate the structure degradation. Furthermore, *ex situ* Raman spectra were acquired on Li_2MnO_3 and LS-LMO before cycling and after the 1st and 50th cycles. As shown in Figure S13a, two broad bands at ~484 and ~604 cm^{-1} can be attributed to the E_g and A_{1g} vibrations of the Raman-active layered structure. The band at ~426 cm^{-1} is considered to be the fingerprint vibration of Li_2MnO_3. Besides, a shoulder band at ~650 cm^{-1} (marked by green arrows) appears in Li_2MnO_3 after the first cycle, which is assigned to the newly formed spinel-like structure.[54,55] The dramatic increase of the shoulder peak after 50 cycles indicates that Li_2MnO_3 almost totally transforms to a spinel-like phase. For LS-LMO, the shoulder peak shows much fewer changes with cycling, confirming that the layered-spinel hybrid structure can be greatly retained (Figure S13b).

In summary, we demonstrated the phase complex engineering in constructing a new high-performance Li–Mn–O cathode for Li-ion batteries, featuring the layered-spinel complex structure coherently at the nanoscale. The introduced spinel nanodomains greatly inhibit the mobility of oxygen

https://doi.org/10.1021/acsenergylett.2c02507
ACS Energy Lett. 2023, 8, 901−908

vacancies in the layered nanodomains at high potentials, allowing the LS-LMO cathode to achieve excellent long-term cycling with an ultrahigh initial capacity of >440 mA h g^{-1} and negligible voltage decay. Our findings show a new class of low-cost and high-performance Li−Mn−O complex cathodes for next-generation Li-ion batteries and verify the potential of the multiphase complex strategy in developing high-performance cathode materials.

■ ASSOCIATED CONTENT

Supporting Information

The Supporting Information is available free of charge at https://pubs.acs.org/doi/10.1021/acsenergylett.2c02507.

Experimental section describing conditions of DFT calculations, material synthesis, material characterizations, TXM measurements, and electrochemical measurements, structural models for DFT calculations, SEM, HRTEM, electrochemical tests, XANES spectra deduced from the corresponding TXM 3D images, and sXAS and HAADF-STEM images, and elemental content and refinement results of XRD and ND data (PDF)

■ AUTHOR INFORMATION

Corresponding Authors

Mingjian Zhang − *School of Advanced Materials, Peking University, Shenzhen Graduate School, Shenzhen 518055, People's Republic of China; School of Science and Engineering, The Chinese University of Hong Kong, Shenzhen 518172, People's Republic of China;* orcid.org/0000-0002-6843-5911; Email: zhangmingjian@cuhk.edu.cn

Mingyuan Ge − *National Synchrotron Light Source II (NSLS-II), Brookhaven National Laboratory, Upton, New York 11973, United States*; Email: mingyuan@bnl.gov

Shunning Li − *School of Advanced Materials, Peking University, Shenzhen Graduate School, Shenzhen 518055, People's Republic of China*; Email: lisn@pku.edu.cn

Lin Xie − *Department of Physics, Southern University of Science and Technology, Shenzhen 518055 Guangdong, People's Republic of China*; Email: xiel3@sustech.edu.cn

Feng Pan − *School of Advanced Materials, Peking University, Shenzhen Graduate School, Shenzhen 518055, People's Republic of China;* orcid.org/0000-0002-8216-1339; Email: panfeng@pkusz.edu.cn

Authors

Weiyuan Huang − *School of Advanced Materials, Peking University, Shenzhen Graduate School, Shenzhen 518055, People's Republic of China*

Zhefeng Chen − *School of Advanced Materials, Peking University, Shenzhen Graduate School, Shenzhen 518055, People's Republic of China*

Gang Wang − *Department of Physics, Southern University of Science and Technology, Shenzhen 518055 Guangdong, People's Republic of China*

Junhao Lin − *Department of Physics, Southern University of Science and Technology, Shenzhen 518055 Guangdong, People's Republic of China;* orcid.org/0000-0002-2195-2823

Jimin Qiu − *School of Advanced Materials, Peking University, Shenzhen Graduate School, Shenzhen 518055, People's Republic of China*

Lei Yu − *Center for Nanoscale Materials, Argonne National Laboratory, Lemont, Illinois 60439, United States*

Jianguo Wen − *Center for Nanoscale Materials, Argonne National Laboratory, Lemont, Illinois 60439, United States;* orcid.org/0000-0002-3755-0044

Guo-Xi Ren − *State Key Laboratory of Functional Materials for Informatics, Shanghai Institute of Microsystem and Information Technology, Chinese Academy of Sciences, Shanghai 200050, People's Republic of China*

Cong Lin − *School of Advanced Materials, Peking University, Shenzhen Graduate School, Shenzhen 518055, People's Republic of China*

Wenguang Zhao − *School of Advanced Materials, Peking University, Shenzhen Graduate School, Shenzhen 518055, People's Republic of China*

Haibiao Chen − *Institute of Marine Biomedicine, Shenzhen Polytechnic, Shenzhen 518055, People's Republic of China*

Complete contact information is available at: https://pubs.acs.org/10.1021/acsenergylett.2c02507

Notes

The authors declare no competing financial interest.

■ ACKNOWLEDGMENTS

This work was financially supported by the National Natural Science Foundation of China (52172175), the Basic and Applied Basic Research Foundation of Guangdong Province (No. 2021B1515130002), the Soft Science Research Project of Guangdong Province (No. 2017B030301013), the Guangdong Innovative and Entrepreneurial Research Team Program (Grant No. 2019ZT08C044), the Shenzhen Science and Technology Research Grant (Nos. JCYJ20200109140416788, JCYJ20210324130812033, and KQTD20190929173815000), and the Major Science and Technology Infrastructure Project of Material Genome Big-science Facilities Platform supported by the Municipal Development and Reform Commission of Shenzhen. This research used the full field X-ray imaging (FXI) beamline (18-ID) of the National Synchrotron Light Source II, a U.S. Department of Energy (DOE) Office of Science User Facility operated for the DOE Office of Science by Brookhaven National Laboratory under Contract No. DE-SC0012704. M.G.'s effort was partially supported by the Laboratory Directed Research and Development (LDRD 20-030) program at Brookhaven National Laboratory. We acknowledge the assistance of the SUSTech Core Research Facilities and the Pico-Centre, which receives support from the Presidential Fund and Development and Reform Commission of Shenzhen Municipality. Work performed at the Center for Nanoscale Materials, a U.S. Department of Energy Office of Science User Facility, was supported by the U.S. DOE, Office of Basic Energy Sciences, under Contract No. DE-AC02-06CH11357.

■ REFERENCES

(1) Tarascon, J.-M.; Armand, M. Issues and challenges facing rechargeable lithium batteries. *Nature* **2001**, *414*, 359−367.

(2) Goodenough, J. B.; Park, K.-S. The Li-ion rechargeable battery: a perspective. *J. Am. Chem. Soc.* **2013**, *135*, 1167−1176.

(3) Song, Y. Z.; Zhao, X. B.; Wang, C.; Bi, H.; Zhang, J.; Li, S. S.; Wang, M.; Che, R. C. Insight into the atomic structure of Li_2MnO_3 in Li-rich Mn-based cathode materials and the impact of its atomic arrangement on electrochemical performance. *J. Mater. Chem. A* **2017**, *5*, 11214−11223.

(4) Liu, H.; Strobridge, F. C.; Borkiewicz, O. J.; Wiaderek, K. M.; Chapman, K. W.; Chupas, P. J.; Grey, C. P. Capturing metastable structures during high-rate cycling of $LiFePO_4$ nanoparticle electrodes. *Science* **2014**, *344*, 1451−1452.
(5) Chung, S.-Y.; Bloking, J. T.; Chiang, Y.-M. Electronically conductive phospho-olivines as lithium storage electrodes. *Nat. Mater.* **2002**, *1*, 123−128.
(6) Tarascon, J. M.; Wang, E.; Shokoohi, F. K.; et al. The spinel phase of $LiMn_2O_4$ as a cathode in secondary lithium cells. *J. Electrochem. Soc.* **1991**, *138*, 2859−2864.
(7) Liu, T. C.; Dai, A.; Lu, J.; Yuan, Y. F.; Xiao, Y. G.; Yu, L.; Li, M.; Gim, J.; Ma, L.; Liu, J. J.; Zhan, C.; Li, L. X.; Zheng, J. X.; Ren, Y.; Wu, T. P.; Shahbazian-Yassar, R.; Wen, J. G.; Pan, F.; Amine, K. Correlation between manganese dissolution and dynamic phase stability in spinel-based lithium-ion battery. *Nat. Commum.* **2019**, *10*, 4721.
(8) Ji, Y. J.; Zhang, P. B.; Lin, M.; Zhao, W. M.; Zhang, Z. R.; Zhao, Y. F.; Yang, Y. Toward a stable electrochemical interphase with enhanced safety on high-voltage $LiCoO_2$ cathode: A case of phosphazene additives. *J. Power Sources* **2017**, *359*, 391−399.
(9) Liu, Q.; Su, X.; Lei, D.; Qin, Y.; Wen, J. G.; Guo, F. M.; Wu, Y. A.; Rong, Y. C.; Kou, R. H.; Xiao, X. H.; Aguesse, F.; Bareño, J.; Ren, Y.; Lu, W. Q.; Li, Y. X. Approaching the capacity limit of lithium cobalt oxide in lithium ion batteries via lanthanum and aluminium doping. *Nat. Energy* **2018**, *3*, 936−943.
(10) Sun, Y.-K.; Myung, S.-T.; Park, B.-C.; Prakash, J.; Belharouak, I.; Amine, K. High-energy cathode material for long-life and safe lithium batteries. *Nat. Mater.* **2009**, *8*, 320−324.
(11) Zheng, J. X.; Ye, Y. K.; Liu, T. C.; Xiao, Y. G.; Wang, C. M.; Wang, F.; Pan, F. Ni/Li disordering in layered transition metal oxide: electrochemical impact, origin, and control. *Acc. Chem. Res.* **2019**, *52*, 2201−2209.
(12) Arico, A. S.; Bruce, P.; Scrosati, B.; Tarascon, J. M.; Schalkwijk, W. V. Nanostructured materials for advanced energy conversion and storage devices. *Nat. Mater.* **2005**, *4*, 366−377.
(13) Luo, K.; Roberts, M. R.; Hao, R.; Guerrini, N.; Pickup, D. M.; Liu, Y.-S.; Edström, K.; Guo, J. H.; Chadwick, A. V.; Duda, L. C.; Bruce, P. Charge-compensation in 3*d*-transition-metaloxide intercalation cathodes through the generation of localized electron holes on oxygen. *Nat. Chem.* **2016**, *8*, 684−691.
(14) McCalla, E.; Abakumov, A. M.; Saubanère, M.; Foix, D.; Berg, E. J.; Rousse, G.; Doublet, M.-L.; Gonbeau, D.; Novák, P.; Tendeloo, G. V.; Dominko, R.; Tarascon, J. M. Visualization of O-O peroxo-like dimers in high-capacity layered oxides for Li-ion batteries. *Science* **2015**, *350*, 1516−1521.
(15) Zhao, S. Q.; Yan, K.; Zhang, J. Q.; Sun, B.; Wang, G. X. Reviving reaction mechanism of layered lithium-rich cathode materials for high-energy lithium-ion battery. *Angew. Chem., Int. Ed.* **2021**, *60* (5), 2208−2220.
(16) Yin, Z. W.; Li, J. T.; Huang, L.; Pan, F.; Sun, S. G. High-capacity Li-rich Mn-based cathodes for lithium-ion batteries. *Chin. J. Struct. Chem.* **2020**, *39*, 20−25.
(17) Li, S. W.; Liu, Z. P.; Yang, L.; Shen, X.; Liu, Q. Y.; Hu, Z. W.; Kong, Q. Y.; Ma, J.; Li, J. D.; Lin, H.-J.; Chen, C.-T.; Wang, X. F.; Yu, R. C.; Wang, Z. X.; Chen, L. Q. Anionic redox reaction and structural evolution of Ni-rich layered oxide cathode material. *Nano Energy* **2022**, *98*, 107335.
(18) Liu, X.; Xu, G.-L.; Kolluru, V. S. C.; Zhao, C.; Li, Q.; Zhou, X.; Liu, Y.; Yin, L.; Zhuo, Z.; Daali, A.; Fan, J.-J.; Liu, W.; Ren, Y.; Xu, W.; Deng, J.; Hwang, I.; Ren, D.; Feng, X.; Sun, C.; Huang, L.; Zhou, T.; Du, M.; Chen, Z.; Sun, S.-G.; Chan, M. K. Y.; Yang, W.; Ouyang, M.; Amine, K. Origin and regulation of oxygen redox instability in high-voltage battery cathodes. *Nat. Energy* **2022**, *7*, 808.
(19) Seo, D.-H.; Lee, J.; Urban, A.; Malik, R.; Kang, S. Y.; Ceder, G. The structural and chemical origin of the oxygen redox activity in layered and cation-disordered Li-excess cathode materials. *Nat. Chem.* **2016**, *8*, 692−697.
(20) Luo, K.; Roberts, M. R.; Hao, R.; Guerrini, N.; Pickup, D. M.; Liu, Y.-S.; Edström, K.; Guo, J. H.; Chadwick, A. V.; Duda, L. C.; Bruce, P. G. Charge-compensation in 3d-transition-metaloxide intercalation cathodes through the generation of localized electron holes on oxygen. *Nat. Chem.* **2016**, *8*, 684−691.
(21) Robertson, A. D.; Bruce, P. Mechanism of electrochemical activity in Li_2MnO_3. *Chem. Mater.* **2003**, *15*, 1984−1992.
(22) Yan, P. F.; Xiao, L.; Zheng, J. M.; Zhou, Y. G.; He, Y.; Zu, X. T.; Mao, S. X.; Xiao, J.; Gao, F.; Zhang, J. G.; Wang, C. M. Probing the degradation mechanism of Li_2MnO_3 cathode for Li-ion batteries. *Chem. Mater.* **2015**, *27*, 975−982.
(23) Zheng, Z.; Weng, M. Y.; Yang, L. Y.; Hu, Z. X.; Chen, Z. F.; Pan, F. Thermodynamically revealing the essence of order and disorder structures in layered cathode materials. *Chin. J. Struct. Chem.* **2019**, *38*, 2020.
(24) Thackeray, M. M.; Kang, S.-H.; Johnson, C. S.; Vaughey, J. T.; Benedek, R.; Hackney, S. A. Li_2MnO_3-stabilized $LiMO_2$ (M = Mn, Ni, Co) electrodes for lithium-ion batteries. *J. Mater. Chem.* **2007**, *17*, 3112−3125.
(25) Zhang, S. M.; Chen, J.; Tang, T.; Jiang, Y. Z.; Chen, G. R.; Shao, Q. N.; Yan, C. H.; Zhu, T. J.; Gao, M. X.; Liu, Y. F.; Pan, H. G. A novel strategy to significantly enhance the initial voltage and suppress voltage fading of a Li- and Mn-rich layered oxide cathode material for lithiumion batteries. *J. Mater. Chem. A* **2018**, *6*, 3610−3624.
(26) Hu, E. Y.; Yu, X. Q.; Lin, R. Q.; Nam, K.-W.; Xin, H. L.; Jaye, C.; Yang, X.-Q.; Bi, X. X.; Lu, J.; Bak, S.; Fischer, D. A.; Amine, K. Evolution of redox couples in Li- and Mn-rich cathode materials and mitigation of voltage fade by reducing oxygen release. *Nat. Energy* **2018**, *3*, 690−698.
(27) Gu, M.; Belharouak, I.; Zheng, J. M.; Wu, H. M.; Xiao, J.; Genc, A.; Amine, K.; Thevuthasan, S.; Baer, D. R.; Zhang, J. G.; Browning, N. D.; Liu, J.; Wang, C. M. Formation of the spinel phase in the layered composite cathode used in Li-ion batteries. *ACS Nano* **2013**, *7*, 760−767.
(28) Yan, P. F.; Nie, A.; Zheng, J. M.; Zhou, Y. G.; Lu, D. P.; Zhang, X. F.; Xu, R.; Belharouak, I.; Zu, X. T.; Xiao, J.; Amine, K.; Liu, J.; Gao, F.; Shahbazian-Yassar, R.; Zhang, J. G.; Wang, C. M. Evolution of lattice structure and chemical composition of the surface reconstruction layer in $Li_{1.2}Ni_{0.2}Mn_{0.6}O_2$ cathode material for lithium ion batteries. *Nano Lett.* **2015**, *15*, 514−532.
(29) Assat, G.; Foix, D.; Delacourt, C.; Iadecola, A.; Dedryvère, R.; Tarascon, J. M. Fundamental interplay between anionic/cationic redox governing the kinetics and thermodynamics of lithium-rich cathodes. *Nat. Commun.* **2017**, *8*, 2219.
(30) Zhuo, Z. Q.; Dai, K. H.; Qiao, R. M.; Wang, R.; Wu, J. P.; Liu, Y. L.; Peng, J. Y.; Chen, L. Q.; Chuang, Y. D.; Pan, F.; Shen, Z. X.; Liu, G.; Li, H.; Devereaux, T. P.; Yang, W. L. Cycling mechanism of Li_2MnO_3: Li-CO_2 batteries and commonality on oxygen redox in cathode materials. *Joule* **2021**, *5* (4), 975−997.
(31) Liu, T. C.; Yu, L.; Liu, J. J.; Lu, J.; Bi, X. X.; Dai, A.; Li, M.; Li, M. F.; Hu, Z. X.; Ma, L.; Luo, D.; Zheng, J. X.; Wu, T. P.; Ren, Y.; Wen, J. G.; Pan, F.; Amine, K. Understanding Co roles towards developing Co-free Ni-rich cathodes for rechargeable batteries. *Nat. Energy* **2021**, *6* (3), 277−286.
(32) Liu, T. C.; Liu, J.; Li, L.; Yu, L.; Diao, J.; Zhou, T.; Li, S.; Dai, A.; Zhao, W.; Xu, S.; Ren, Y.; Wang, L.; Wu, T.; Qi, R.; Xiao, Y.; Zheng, J.; Cha, W.; Harder, R.; Robinson, I.; Wen, J.; Lu, J.; Pan, F.; Amine, K. Origin of structural degradation in Li-rich layered oxide cathode. *Nature* **2022**, *606* (7913), 305.
(33) Wu, F.; Li, N.; Su, Y. F.; Shou, H. F.; Bao, L. Y.; Yang, W.; Zhang, L. J.; An, R.; Chen, S. Spinel/layered heterostructured cathode material for high-capacity and high-rate Li-ion batteries. *Adv. Mater.* **2013**, *25*, 3722−3726.
(34) Liu, J. X.; Wang, J. Q.; Ni, Y. X.; Zhang, Y. D.; Luo, J.; Cheng, F. Y.; Chen, J. Spinel/lithium-rich manganese oxide hybrid nanofibers as cathode materials for rechargeable lithium-ion batteries. *Small Methods* **2019**, *3*, 1900350.
(35) Li, Q. Y.; Zhou, D.; Zhang, L. J.; Ning, D.; Chen, Z. H.; Xu, Z. J.; Gao, R.; Liu, X. Z.; Xie, D. H.; Schumacher, G.; Liu, X. F. Tuning anionic redox activity and reversibility for a high-capacity Li-rich Mn-

based oxide cathode via an integrated strategy. *Adv. Funct. Mater.* **2019**, *29*, 1806706.

(36) Wu, F.; Li, N.; Su, Y. F.; Zhang, L. J.; Bao, L. Y.; Wang, J.; Chen, L.; Zheng, Y.; Dai, L. Q.; Peng, J. Y.; Chen, S. Ultrathin spinel membrane-encapsulated layered lithium-rich cathode material for advanced Li-ion batteries. *Nano Lett.* **2014**, *14*, 3550−3555.

(37) Zhang, X. D.; Shi, J. L.; Liang, J. Y.; Yin, Y. X.; Zhang, J. N.; Yu, X. Q.; Guo, Y. G. Suppressing surface lattice oxygen release of Li-rich cathode materials via heterostructured spinel $Li_4Mn_5O_{12}$ coating. *Adv. Mater.* **2018**, *30*, 1801751.

(38) Zhu, Z.; Yu, D. W.; Shi, Z.; Gao, R.; Xiao, X. H.; Waluyo, I.; Ge, M. Y.; Dong, Y. H.; Xue, W. J.; Xu, G. Y.; Lee, W.-K.; Huntb, A.; Li, J. Gradient-morph $LiCoO_2$ single crystals with stabilized energy density above 3400 W h L^{-1}. *Energy Environ. Sci.* **2020**, *13*, 1865−1878.

(39) Lei, C.H.; Bareno, J.; Wen, J.G.; Petrov, I.; Kang, S.-H.; Abraham, D.P. Local structure and composition studies of $Li_{1.2}Ni_{0.2}Mn_{0.6}O_2$ by analytical electron microscopy. *J. Power Sources* **2008**, *178*, 422−433.

(40) Wen, J. G.; Bareño, J.; Lei, C. H.; Kang, S.-H.; Balasubramanian, M.; Petrov, I.; Abraham, D. P. Analytical electron microscopy of $Li_{1.2}Co_{0.4}Mn_{0.4}O_2$ for lithium-ion batteries. *Solid State Ionics* **2011**, *182*, 98−107.

(41) Zhu, X. H.; Meng, F. Q.; Zhang, Q. H.; Xue, L.; Zhu, H.; Lan, S.; Liu, Q.; Zhao, J.; Zhuang, Y. H.; Guo, Q. B.; Liu, B.; Gu, L.; Lu, X.; Ren, Y.; Xia, H. $LiMnO_2$ cathode stabilized by interfacial orbital ordering for sustainable lithium-ion batteries. *Nat. Sustain.* **2021**, *4* (5), 392−401.

(42) Huang, W. Y.; Yang, L. Y.; Chen, Z. F.; Liu, T. C.; Ren, G. X.; Shan, P. Z.; Zhang, B.-W.; Chen, S. M.; Li, S. N.; Li, J. Y.; Lin, C.; Zhao, W. G.; Qiu, J. M.; Fang, J. J.; Zhang, M. J.; Dong, C.; Li, F.; Yang, Y.; Sun, C.-J.; Ren, Y.; Huang, Q. Z.; Hou, G. J.; Dou, S.-X.; Lu, J.; Amine, K.; Pan, F. Elastic lattice enabling reversible tetrahedral Li storage sites in a high-capacity manganese oxide cathode. *Adv. Mater.* **2022**, *34*, 2202745.

(43) Lyu, Y.; Hu, E.; Xiao, D.; Wang, Y.; Yu, X.; Xu, G.; Ehrlich, S. N.; Amine, K.; Gu, L.; Yang, X.-Q.; Li, H. Correlations between transition-metal chemistry, local structure, and global structure in $Li_2Ru_{0.5}Mn_{0.5}O_3$ investigated in a wide voltage window. *Chem. Mater.* **2017**, *29*, 9053−9065.

(44) Yin, W.; Grimaud, A.; Rousse, G.; Abakumov, A. M.; Senyshyn, A.; Zhang, L. T.; Trabesinger, S.; Iadecola, A.; Foix, D.; Giaume, D.; Tarascon, J.-M. Structural evolution at the oxidative and reductive limits in the first electrochemical cycle of $Li_{1.2}Ni_{0.13}Mn_{0.54}Co_{0.13}O_2$. *Nat. Commun.* **2020**, *11*, 1252.

(45) Rana, J.; Papp, J. K.; Lebens-Higgins, Z.; Zuba, M.; Kaufman, L. A.; Goel, A.; Schmuch, R.; Winter, M.; Whittingham, M. S.; Yang, W. L.; McCloskey, B. D.; Piper, L. F. J. Quantifying the capacity contributions during activation of Li_2MnO_3. *ACS Energy Lett.* **2020**, *5* (2), 634−641.

(46) Li, B.; Yan, H. J.; Ma, J.; Yu, P. R.; Xia, D. G.; Huang, W. F.; Chu, W. S.; Wu, Z. Y. Manipulating the electronic structure of Li-rich manganese-based oxide using polyanions: towards better electrochemical performance. *Adv. Funct. Mater.* **2014**, *24*, 5112−5118.

(47) Ge, M. Y.; Coburn, D. S.; Nazaretski, E.; Xu, W. H.; Gofron, K.; Xu, H. J.; Yin, Z. J.; Lee, W. K. One-minute nano-tomography using hard X-ray full-field transmission microscope. *Appl. Phys. Lett.* **2018**, *113* (8), 083109.

(48) Sathiya, M.; Rousse, G.; Ramesha, K.; Laisa, C. P.; Vezin, H.; Sougrati, M. T.; Doublet, M.-L.; Foix, D.; Gonbeau, D.; Walker, W.; Prakash, A. S.; Ben Hassine, M.; Dupont, L.; Tarascon, J.-M. Reversible anionic redox chemistry in high-capacity layered-oxide electrodes. *Nat. Mater.* **2013**, *12*, 827−835.

(49) Li, B.; Kumar, K.; Roy, I.; Morozov, A. V.; Emelyanova, O. V.; Zhang, L. T.; Koo, T.; Belin, S.; Cabana, J.; Dedryvère, R.; Abakumov, A. M.; Tarascon, J.-M. Capturing dynamic ligand-to-metal charge transfer with a long-lived cationic intermediate for anionic redox. *Nat. Mater.* **2022**, *21*, 1165−1174.

(50) Lun, Z. Y.; Ouyang, B.; Cai, Z. J.; Clément, R. J.; Kwon, D.-H.; Huang, J. P.; Papp, J. K.; Balasubramanian, M.; Tian, Y. S.; McCloskey, B. D.; Ji, H. W.; Kim, H.; Kitchaev, D. A.; Ceder, G. Design principles for high-capacity Mn-based cation-disordered rocksalt cathodes. *Chem.* **2020**, *6*, 153−168.

(51) Yan, P. F.; Zheng, J. M.; Tang, Z.-K.; Devaraj, A.; Chen, G. Y.; Amine, K.; Zhang, J.-G.; Liu, L.-M.; Wang, C. M. Injection of oxygen vacancies in the bulk lattice of layered cathodes. *Nat. Nanotechnol.* **2019**, *14*, 602−608.

(52) Yan, P.; Xiao, L.; Zheng, J.; Zhou, Y.; He, Y.; Zu, X.; Mao, S. X.; Xiao, J.; Gao, F.; Zhang, J.-G.; Wang, C.-M. Probing the degradation mechanism of Li_2MnO_3 cathode for Li-ion batteries. *Chem. Mater.* **2015**, *27*, 975−982.

(53) Zheng, J. M.; Gu, M.; Xiao, J.; Zuo, P. J.; Wang, C. M.; Zhang, J. G. Corrosion/fragmentation of layered composite cathode and related capacity/voltage fading during cycling process. *Nano Lett.* **2013**, *13*, 3824−3830.

(54) Lin, M.-H.; Cheng, J.-H.; Huang, H.-F.; Chen, U-F.; Huang, C.-M.; Hsieh, H.-W.; Lee, J.-M.; Chen, J.-M.; Su, W.-N.; Hwang, B.-J. Revealing the mitigation of intrinsic structure transformation and oxygen evolution in a layered $Li_{1.2}Ni_{0.2}Mn_{0.6}O_2$ cathode using restricted charging protocols. *J. Power Source* **2017**, *359*, 539−548.

(55) Deng, Y.-P.; Fu, F.; Wu, Z.-G.; Yin, Z.-W.; Zhang, T.; Li, J.-T.; Huang, L.; Sun, S.-G. Layered/spinel heterostructured Li-rich materials synthesized by a one-step solvothermal strategy with enhanced electrochemical performance for Li ion batteries. *J. Mater. Chem. A* **2016**, *4*, 257−263.

https://doi.org/10.1021/acsenergylett.2c02507
ACS Energy Lett. 2023, 8, 901−908